Journal of Materials Chemistry A

Understanding high photocatalytic activity of TiO2 high-pressure columbite phase by experiments and first-principles calculations

SCHOLARONE™
Manuscripts

Understanding high photocatalytic activity of TiO₂ high-pressure columbite phase by experiments and first-principles calculations

Jacqueline Hidalgo-Jiménez[a,b], Taner Akbay[c], Tatsumi Ishihara[a,d,e] and Kaveh Edalati[a,b,e,*]

The clean production of hydrogen as a zero-emission fuel can be done using photocatalysis, with TiO₂ being one of the most promising photocatalysts. However, the activity of TiO₂ anatase and rutile phases is still limited. In this study, an oxygen-deficient high-pressure phase of TiO₂, columbite, is stabilized by a high-pressure torsion method. The phase is utilized as an active photocatalyst for hydrogen production, and the mechanism of its high activity is examined by density functional theory (DFT). The activity of columbite appears to be experimentally higher than the anatase phase. DFT calculations revealed that columbite does not have a narrow electronic bandgap, but its optical bandgap and light absorbance improve by oxygen vacancies more significantly compared to anatase. Moreover, the water adsorption energy is higher and the surface activation energy for water splitting on the (101) atomic plane of columbite is lower than that for the active planes of anatase. In conclusion, although columbite is not a low-bandgap semiconductor, its large light absorbance and high surface catalytic activity make it a promising candidate for photocatalytic reactions.

Introduction

CO₂ emission due to rapid economic growth has become a major problem in the last few decades. Some of the most polluting activities in our daily life are related to the use of fossil fuels such as in transportation and energy conversion units. In order to reduce CO₂ emissions, hydrogen can play a crucial role by reducing the use of fossil fuels[1]. However, hydrogen is mainly produced by steam reforming which generates a significant amount of CO₂ during the process. Therefore, photocatalysis has been considered one of the most promising alternatives for hydrogen production[2].

Among many semiconductor photocatalysts, TiO₂ is the first and one of the most efficient[3]. In TiO₂ photocatalysis, the oxidation reaction of water for hydrogen evolution occurs by photogenerated charge carriers[3]. Rutile and anatase, with tetragonal crystal structures (Fig. 1(a))[4], are the main TiO₂ phases utilized for photocatalysis[1-3]. However, the wide bandgap of these phases being ~3.0 eV for rutile and ~3.2 eV for anatase (i.e. difficult electron-hole generation) and their easy electron-hole recombination limit their photocatalytic performance[5]. TiO₂ has a high-pressure columbite phase, with the orthorhombic crystal structure (Fig. 1(a)) which has received limited attention as a catalyst due to the difficulty in stabilizing it at ambient pressure[6,7].
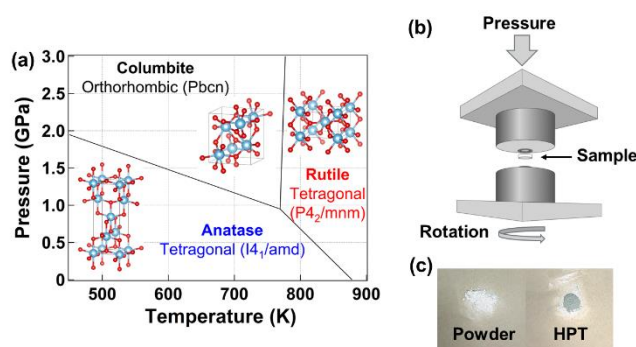

Fig. 1. (a) Phase diagram of TiO₂, (b) schematic representation of HPT and (c) appearance of TiO₂ pristine powder and sample processed by HPT.

In this study, a large fraction of the columbite phase is experimentally stabilized by a high-pressure torsion (HPT) process (Fig. 1(b))[8]. The high photocatalytic activity of the high-pressure phase for hydrogen production is experimentally shown and the mechanism of high photocatalytic activity is theoretically examined by using density functional theory (DFT) calculations for the first time.

Materials and Methods

Both experiments and DFT calculations were employed in this study to clarify the impact of the columbite high-pressure phase on photocatalytic activity.

Experimental Procedures

Sample preparation

a. WPI, International Institute for Carbon-Neutral Energy Research (WPI-I2CNER), Kyushu University, Fukuoka, Japan
b. Graduate School of Integrated Frontier Sciences, Department of Automotive Science, Kyushu University, Fukuoka, Japan
c. Department of Materials Science and Nanotechnology Engineering, Yeditepe University, Istanbul, Turkey
d. Department of Applied Chemistry, Faculty of Engineering, Kyushu University, Fukuoka, Japan
e. Mitsui Chemicals, Inc. - Carbon Neutral Research Center (MCI-CNRC), Kyushu University, Fukuoka, Japan

It was attempted to generate columbite as much as possible using the HPT method. The initial powder utilized was TiO_2 anatase powder (99.8%). About 260 mg of powder was first pressed under 30 kN to generate a 10 mm disc which was later processed by HPT under a pressure of 6 GPa at room temperature. The rotation applied for HPT was 15 turns and the rotation speed was 1 rpm. The resulting material, which had a disc shape with 10 mm diameter and 0.8 mm thickness, was then crushed using a mortar and pestle, and used for characterization and photocatalytic test. The appearance of the sample before and after HPT processing is shown in Fig 1(c), indicating that the color of the HPT-processed sample is gray which is an indication of the formation of color centers such as oxygen vacancies[9].

Characterization

The phase transformation and crystal structure changes were examined by X-ray diffraction (XRD) using Cu Kα radiation, followed by Raman spectroscopy using a laser source of 532 nm wavelength.

The microstructure of the TiO_2 samples was studied by scanning electron microscopy (SEM) using an acceleration voltage of 15 keV and transmission electron microscopy (TEM) using an acceleration voltage of 200 keV. Bright-field (BF), selected area electron diffraction (SAED) and high-resolution imaging techniques were utilized to study the microstructural features.

The formation of oxygen vacancies was evaluated by X-ray photoelectron spectroscopy (XPS) using a radiation source of Mg Kα.

The optical characteristics were examined by photoluminescence (PL) emission spectroscopy with a 325 nm laser source. UV-vis spectroscopy was utilized to study the light absorbance of the samples, followed by a bandgap estimation by the Kubelka-Munk theory[10]. XPS was used to estimate the top of the valence bad, and finally, the band structure was studied by combining the UV-vis spectroscopy and XPS data, as described in detail in an earlier publication[9].

Photocatalytic Activity Measurement

The photocatalytic activity for hydrogen production from water decomposition on the TiO_2 powder and HPT-treated sample was analyzed under a full light arc of a 300 W UV Xe source. For the sample preparation, 50 mg of the sample, 27 mL of H_2O, 3 mL of methanol (as a sacrificial agent), and 0.25 mL of $H_3PtCl_6.6H_2O$ (0.01 M) were mixed. The photocatalytic test was conducted for a single cycle of 180 minutes, in which the amount of hydrogen was measured every 30 minutes.

Computational Methods

To clarify the possible mechanisms underlying the photocatalytic activity of the columbite phase, three main points were theoretically investigated: (1) the electronic bandgap of the columbite phase of TiO_2, (2) the effect of oxygen vacancies in columbite on the reduction of optical bandgap, and (3) the surface activity of columbite phase of TiO_2 for water splitting. These points were studied by first-principles calculations using density functional theory (DFT). All calculations were performed in the plane wave DFT formalism

as implemented in the Vienna *Ab-initio* Simulation Package (VASP)[11,12]. Generalized gradient approximation (GGA) was utilized together with the Perdew-Burke-Ernzerhof (PBE) functional to describe the exchange correlation. Projected-augmented wave (PAW)[13] pseudo potential described 12 valence electrons for titanium ($3p^6$ $4s^2$ $3d^4$), 6 electrons for oxygen ($2s^2$ $2p^4$) and 1 electron for hydrogen. The wave functions were expanded with a cutoff energy of 520 eV. The Brillouin zone was sampled with an optimized number of K points according to the geometric nature of the structure. The graphical visualization was made by utilizing VESTA software[14].

Estimation of Hubbard U-Term

Since DFT underestimates the bandgap due to the coulomb interaction effects, the Hubbard U parameter was included in the calculations. For the selection of U value, five TiO_2 polymorphs, rutile (tetragonal, P42/mnm), anatase (tetragonal, I41/amd), brookite (orthorhombic, Pcab), columbite (orthorhombic, Pbcn) and baddeleyite (monoclinic, P21/c), were evaluated with different U values. For these calculations, all structures were made of 12 atoms (4 Ti and 8 O). Then, the obtained bandgaps were compared with reported experimental results for rutile, anatase and brookite. These comparisons suggested that $U = 8$ eV is a reasonable value for all polymorphs.

Oxygen Vacancy Effect on Optical Bandgap

Supercells of anatase and columbite with 96 atoms (32 Ti and 64 O) were studied with different concentrations of oxygen vacancies: 3% (2 out of 64 O atoms were removed) and 6% (4 out of 64 O atoms were removed). These supercells were optimized before the self-consistent field (SCF) calculations and used for the calculation of density of states (DOS), band structure and vacancy formation energy. The k-point grid utilized for anatase and columbite supercells were 8×8×6 and 8×8×8, respectively.

Surface Activation Energy for Water Splitting

Several columbite surface slabs (atomic planes) were generated by utilizing the code Surfaxe[15] with 15 Å of vacuum and 10 Å of bulk and with zero net electrostatic dipole moments. From several slabs, (011) and (101) atomic planes were selected because of their reported high activity in other TiO_2 polymorphs[16–19]. The (011) surface termination consisted of four-coordinated and five-coordinated titanium atoms and two-coordinated and one-coordinated oxygen atoms. Comparatively, the (101) surface termination consisted of five-coordinated titanium and one-coordinated and three-coordinated oxygen atoms. These optimizations were performed utilizing the electronic convergence criteria of $1.0×10^{-5}$ eV and the ionic relaxation force criteria of 0.03 eV/Å. Both Brillouin zones were sampled with a 4×4×1 k-point grid.

On the (011) and (101) surface slabs, the water molecule was set above a five-coordinated titanium atom placed near the center of the slab to perform the first optimization calculation (molecular adsorption). Then, for the dissociation mechanism, the closest one-coordinated oxygen was selected to bond with the nearest hydrogen that was separated from the water molecule, and optimization calculations were carried out. Finally, the nudged elastic band (NEB) and climbing image

nudged elastic band (CiNEB) methods[20] were used for finding saddle points and the minimum energy path between the molecular adsorption and dissociative states. The number of intermediate steps along each reaction pathway was set to three. Density functional perturbation theory (DFPT) was also employed to study the phonon dispersion curves and the dynamic stability of the saddle points structures by using the code Phonopy[21].

Experimental Results

Phase Transformations

HPT can generate multiple changes in the microstructure of the processed materials[8,22]. One of them is the stabilization of high-pressure phases, such as columbite[4]. XRD patterns of the powder and the HPT-processed sample are shown in Fig. 2(a). The initial powder is composed of mainly the anatase phase with a small amount of the rutile phase (~3 wt%). The XRD pattern for the HPT-processed sample shows a significant increase in the columbite fraction. Phase analysis by the PDXL2 software indicates that the fraction of the anatase, rutile and columbite phases after HPT processing reaches ~2 wt%, ~29

wt% and ~69 wt%, respectively. Peak broadening also occurs after HPT processing which is related to the reduction in the crystallite size and the formation of crystal defects such as dislocations[22]. The crystallite size refinement permits the columbite phase to remain stable after releasing the pressure because of increasing the energy barrier for the nucleation of rutile or anatase phases[6].

In Fig. 2(b), the differences between the center and the edge of the sample processed by HPT are compared with the initial powder using Raman spectroscopy. The initial powder shows only the peaks for the anatase phase. For the HPT-treated disc, the anatase phase appears near the center; however, the anatase traces almost disappear when the measurements are taken close to the edge. Near to edge, the peaks related to columbite, and rutile phases became more intense because the shear strain is much higher in this region[8].

Microstructure Evolution

SEM micrographs are shown in Fig. 3 for (a) anatase powder and (b) sample processed by HPT. These micrographs show the different characteristics of both samples and confirm the partial consolidation of the powders occur as a result of the HPT
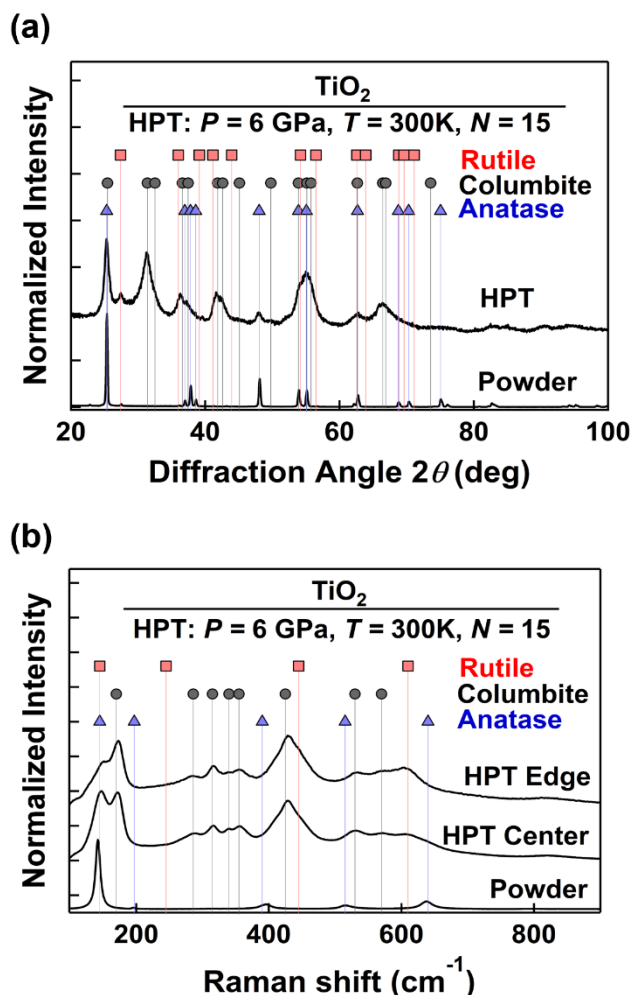

Fig. 2. Columbite phase formation by HPT processing. (a) XRD patterns and (b) Raman spectra obtained for TiO_2 after processing in comparison with initial anatase powder.
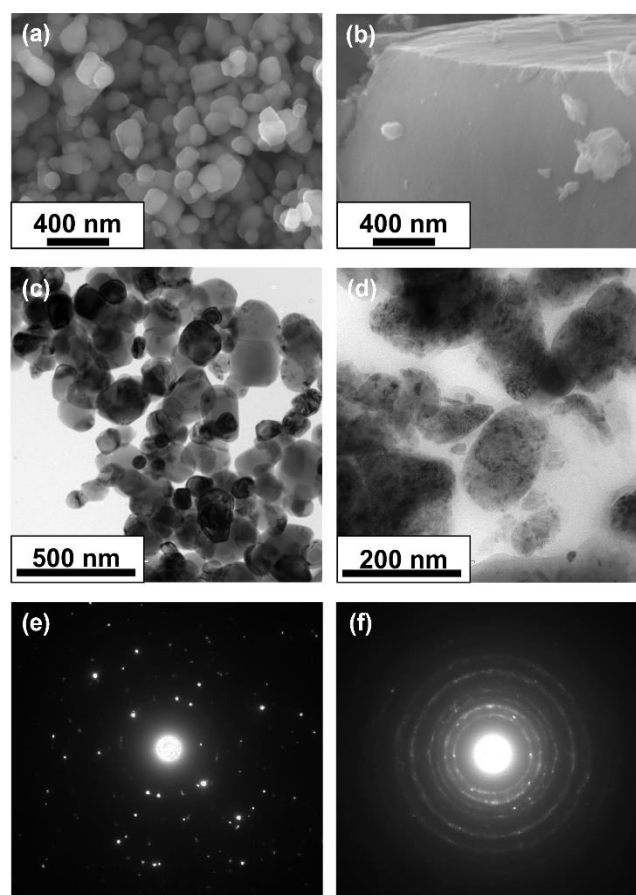

Fig. 3. Partial consolidation and crystal size reduction in TiO_2 after HPT processing. (a, b) SEM micrographs, (c, d) TEM-BF images and (e, f) SAED patters for (a, c, e) TiO_2 powder and (b, d, f) sample processed by HPT.

process[23]. Based on the SEM images, the average particle size of samples was determined as 114 nm for the anatase powder and 14.0 µm for the HPT-processed sample. Consolidation of oxide powders by HPT is a consequence of high applied pressure and concurrent shear strain, as discussed earlier for various oxides[23].

Fig. 3 shows the microstructural characteristics of (c, e) initial powder and (d, f) HPT-processed sample examined by (c, d) TEM-BF and (e, f) SAED modes. Despite the partial powder consolidation by HPT, some dark contrasts appear within the particles which should be due to the formation of nanocrystals and/or lattice defects. The change in the shape of the SAED analysis from a dotted pattern to a ring pattern also demonstrates the reduction in the crystal size from the original powder to the HPT-processed sample. The formation of nanograins is due to the effect of severe plastic deformation induced by the HPT process[8,22].

The HR-TEM images in Fig. 4 were used to examine the nanostructural features of the samples more clearly. These images confirm the presence of the high-pressure phase columbite in the HPT-processed sample, as shown in Fig. 4(a). Additionally, a large amount of grain and interphase boundaries, such as the one in Fig. 4(b), are formed due to the

reduction in grain size to the nanometer level. Furthermore, the examination of the micrographs confirms the formation of dislocation-based defects such as Lomer-Cottrell locks, as shown in Fig. 4(c). This type of defect occurs particularly in crystalline materials when a dislocation encounters another dislocation[24]. The presence of these nanograins and dislocations are in good agreement with the XRD peak broadening observed in Fig. 2(a). The formation of boundaries between the TiO_2 phases is expected to act as heterojunctions for easy electron-hole separation during light irradiation[25,26].

XPS measurements were used to examine the formation of oxygen vacancies, as shown in Fig. 5 for (a) Ti $2p_{1/2}$ and (b) O 1s. After HPT processing, the spectra for Ti $2p_{1/2}$ shows a small extension to lower binding energies while the spectra for O 1s slightly extends to higher energies. These changes confirm that oxygen vacancies are formed after HPT processing. The formation of oxygen vacancies is consistent with the gray color of the HPT-processed sample in Fig. 1c. It should be noted that the concentration of vacancies can be enhanced in the HPT process by either increasing the applied strain (i.e. increasing the number of rotations)[27] or increasing the processing temperature[9,28].
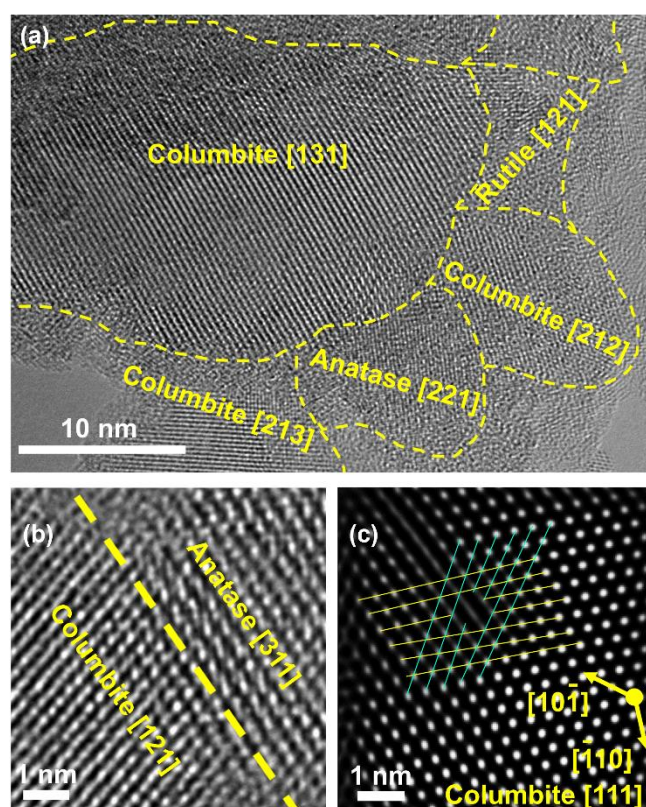

Fig. 4. Formation of nanocrystals and crystal lattice defects in TiO_2 after HPT processing. (a) TEM-HR micrograph, (b) lattice image of phase boundary, and (c) lattice image of dislocation Lomer-Cottrell lock defect reconstructed by inverse fast Fourier transform for HPT-processed sample.
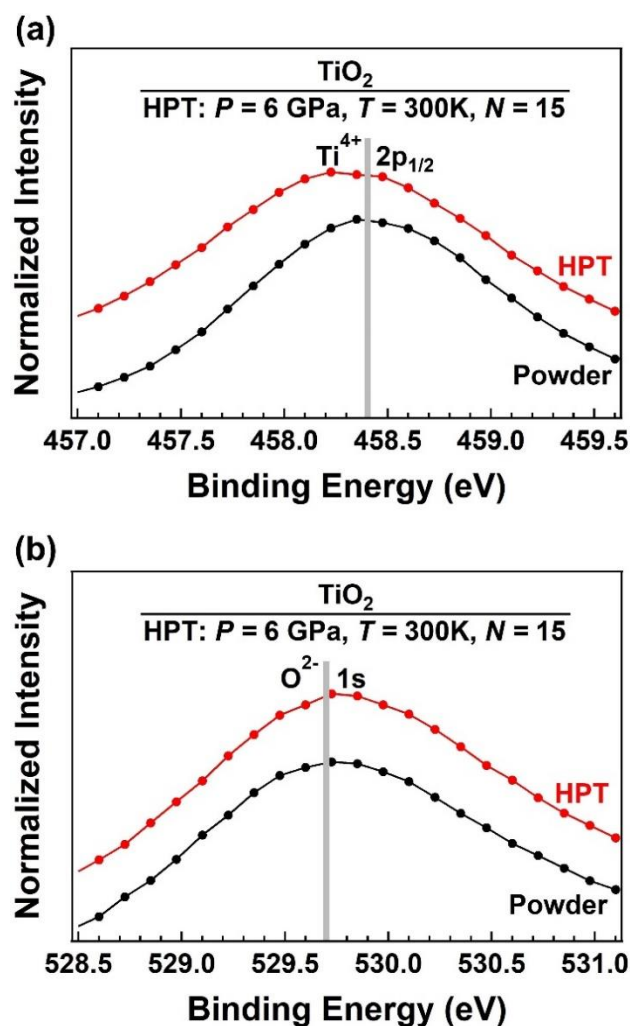

Fig. 5. Formation of oxygen vacancies in TiO_2 after HPT processing. XPS profiles of (a) Ti $2p_{1/2}$ and (b) O 1s after HPT processing in comparison with initial anatase powder.
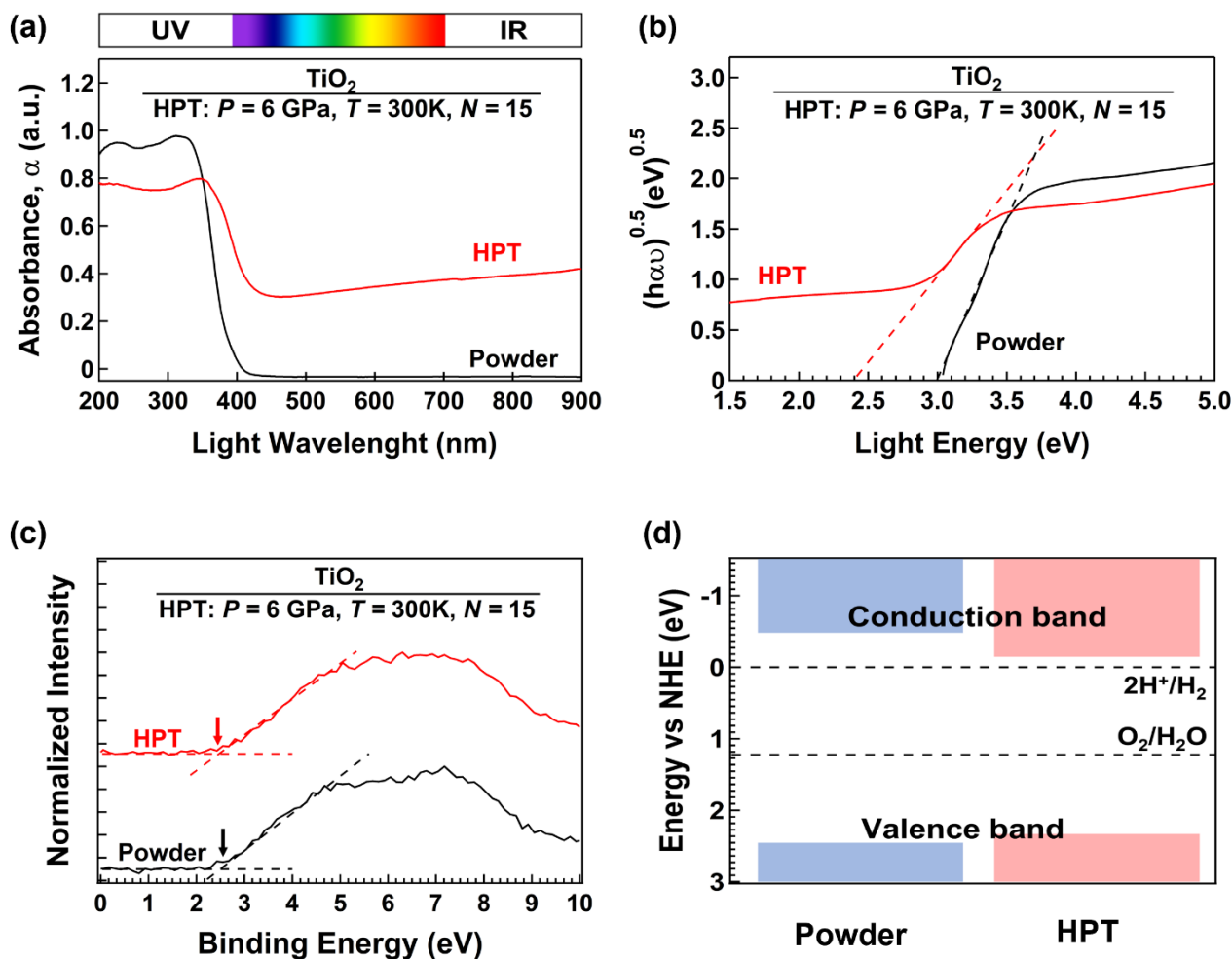
Fig. 6. Enhancement of light absorbance and optical bandgap reduction after HPT processing. (a) UV-vis spectroscopy, (b) Kubelka-Munk analysis for bandgap calculation, (c) XPS spectra for valence band top calculation and (d) band structure obtained for HPT-treated TiO_2 in comparison with initial anatase powder.

Optical Properties

To examine the optical properties of samples, multiple methods were utilized. First, UV-vis spectroscopy and the Kubelka-Munk method were employed to analyze the light absorbance and the bandgap of the material. The UV-vis spectra are shown in Fig. 6(a), indicating that the light absorbance is higher for the HPT-processed sample. Moreover, as shown in Fig. 6(b), TiO_2 exhibits a reduction in the optical bandgap after HPT processing. The initial powder has a bandgap of 3 eV, while the bandgap of the sample processed by HPT is 2.4 eV. The enhancement in the light absorbance after HPT processing was also reported in other HPT-processed oxides and attributed to phase transformations and/or lattice defect generation[9,27,28].

Both samples were analyzed by XPS in order to understand their valence bad structure. Fig. 6(c) shows the XPS data to determine the top of the valence band. The valence band top for the powder and the HPT-processed sample is 2.5 and 2.3 eV vs NHE, respectively. By considering the bandgap and the valence band top energy, the bottom of the conduction band is
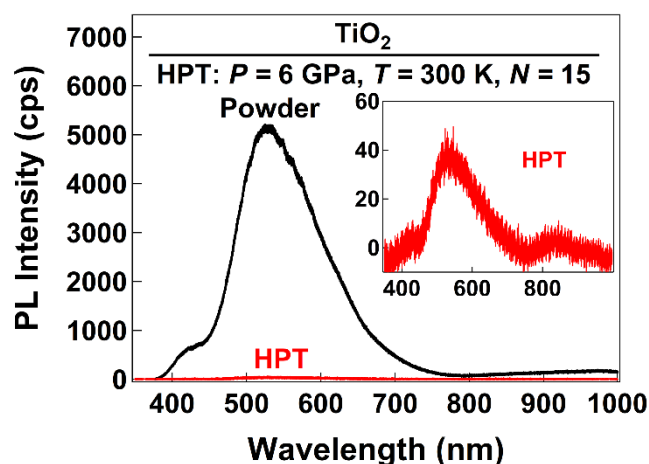

Fig. 7. Reduction of charge carrier recombination after HPT processing. PL emission spectra for TiO_2 after HPT processing in comparison with initial anatase powder.

(a)

TiO$_2$
HPT: P = 6 GPa, T = 300K, N = 15

HPT

Powder

(b)

TiO$_2$
HPT: P = 6 GPa, T = 300K, N = 15
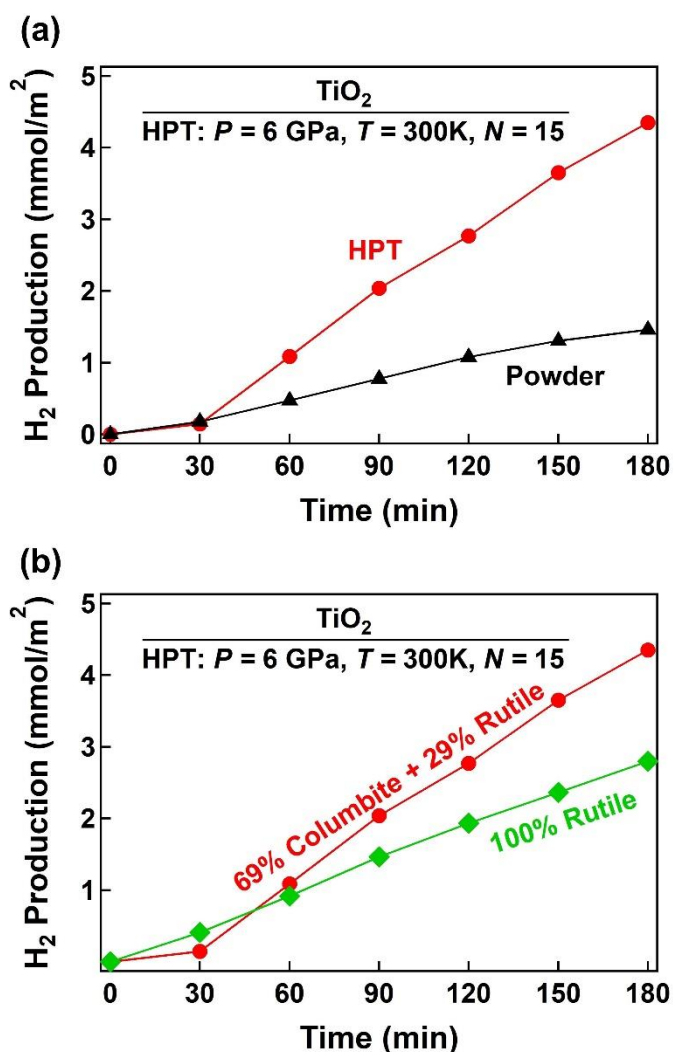
69% Columbite + 29% Rutile

100% Rutile

Fig. 8. Enhancement of photocatalytic hydrogen evolution after HPT processing. Hydrogen produced per surface area of catalyst versus irradiation time under UV light for (a) anatase powder before and after HPT processing and (b) HPT-processed anatase (containing 69 wt% columbite, 29 wt% rutile and 2 wt% anatase) and rutile (containing 100% rutile).

TiO$_2$
HPT: P = 6 GPa, T = 300K, N = 15
After photocatalytic test

Rutile
Columbite
Anatase

HPT

Powder

Fig. 9. Stability of TiO$_2$ photocatalysts. XRD profiles after photocatalytic test for anatase powder and HPT-processed TiO$_2$.

Exp. Brookite
Exp. Anatase
Exp. Rutile

Anatase
Rutile
Brookite
Columbite
Baddeleyite

Fig. 10. Large electronic bandgap of high-pressure columbite phase. Variation of electronic bandgap with U values of 0 to 9 for anatase, rutile, brookite, columbite and baddeleyite. Horizontal lines at 3.0, 3.2 and 3.4 eV indicate reported experimental bandgaps for rutile, anatase, and brookite, respectively.

calculated as -0.5 eV vs NHE for the anatase powder and -0.15 eV vs NHE for the HPT-processed sample. The electronic band structure is summarized in Fig. 6(d), showing that both powder and HPT-processed samples satisfy the thermodynamic requirements for water splitting[1-3].

The PL spectroscopy measurement was utilized to study the recombination of the charge carriers. In Fig. 7, the PL intensity drastically decreases after the HPT process. For the initial powder, one peek at ~510 nm is detected which is associated with oxygen vacancies and shallow bulk traps of anatase[7,29]. These results indicate that the radiative recombination of the carriers is significantly decreased by the utilization of HPT, which is a positive feature for photocatalysis[1-3].
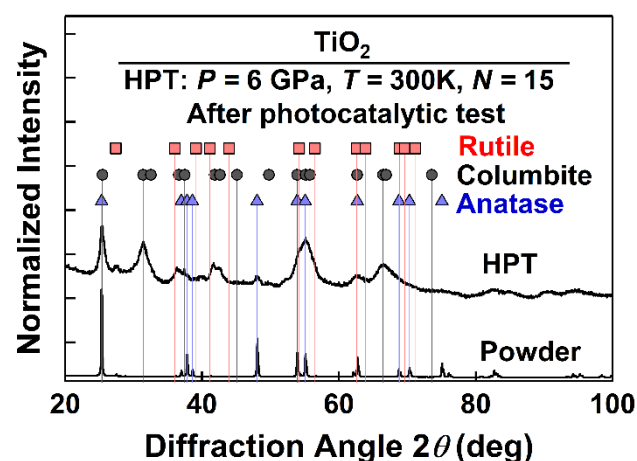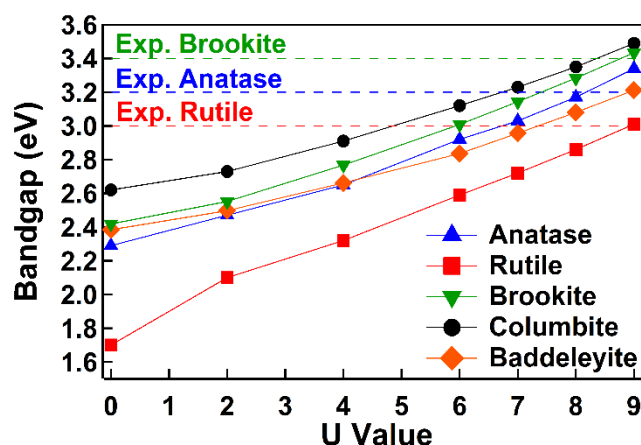
Photocatalytic Activity

The photocatalytic activity of samples was tested for hydrogen production under the full arc of Xe light. Fig. 8(a) shows a comparison of the photocatalytic activity of the initial powder and the HPT-processed sample. The photocatalytic activity was normalized by surface area, calculated from the particle sizes obtained by the SEM analysis, in order to have a reasonable comparison. The HPT-processed sample have a higher activity than the initial powder, and the photocatalytic hydrogen production obtained for this sample is almost 4 times better than the initial powder. These results show that the stabilization of columbite with lattice defects such as oxygen vacancies and dislocations can improve the photocatalytic activity. Since the HPT-processed sample contains not only the columbite phase but also 29 wt% of defective rutile phase, an additional photocatalytic test was conducted on rutile processed by HPT for 15 turns under 6 GPa and at room temperature to confirm whether the high activity is due to the presence of defective
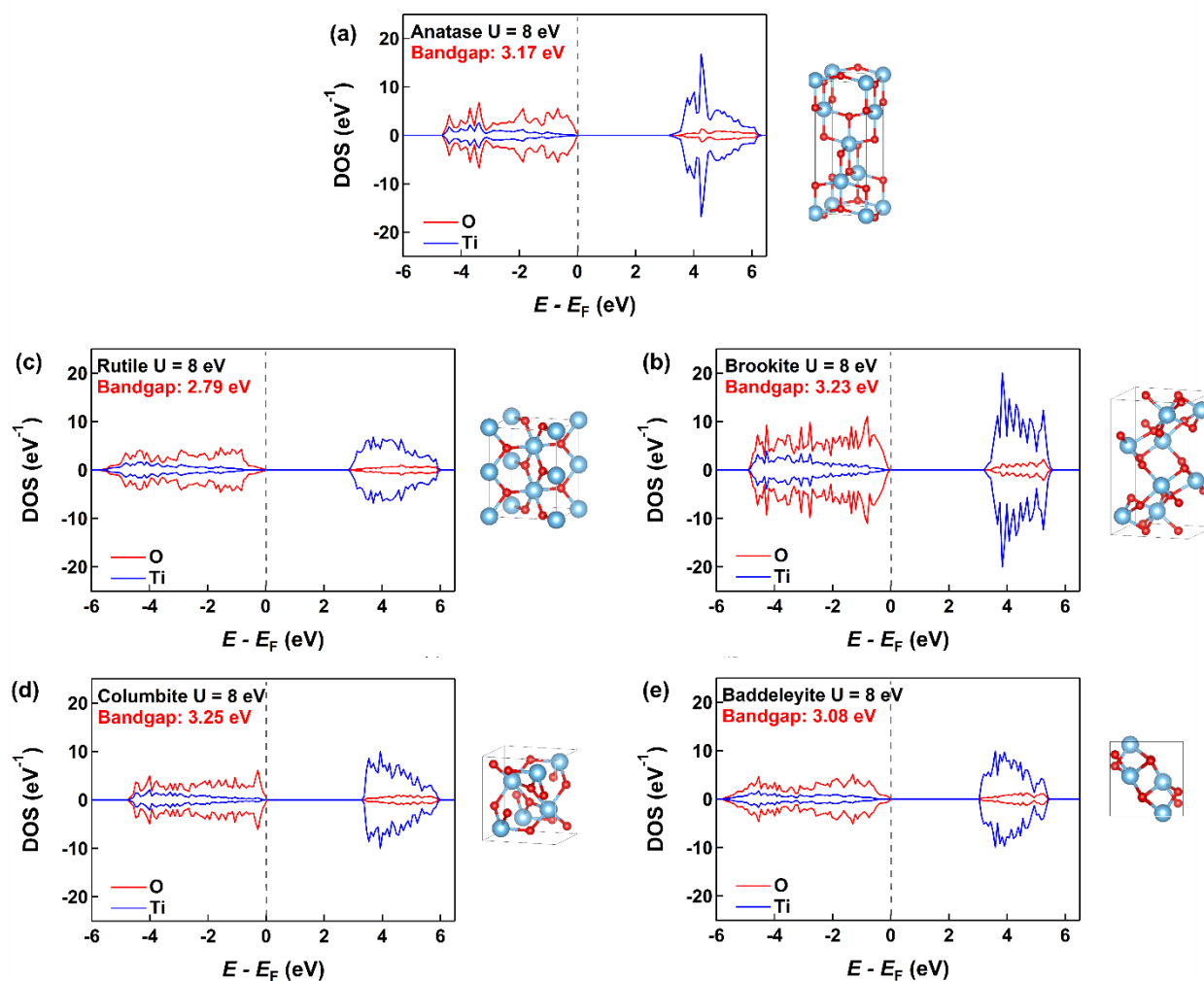
Fig. 11. Contribution of oxygen to valence band top and of titanium to conduction band bottom in TiO_2 polymorphs. Calculated DOS using U value of 8 eV for (a) anatase (b), rutile (c) brookite, (d) columbite and (e) baddeleyite.

columbite or rutile. As shown in Fig. 8(b), defective rutile phase, which did not show any phase transformation by HPT, has a good activity, but its activity does not reach the activity of sample containing 69 wt% of columbite. It is concluded that the formation of defective columbite phase is the main reason for the improvement of photocatalytic activity in this study. Such improvement should be due to higher light absorbance, lower electron-hole recombination rate and higher fractions of active sites (e.g. heterojunctions, dislocations or vacancies)[6,7].

The stability of the material was also evaluated by XRD after the photocatalytic test. The XRD results are plotted in Fig. 9. These XRD profiles show no changes compared to the previously shown patterns in Fig. 2(a) before the photocatalytic test, demonstrating the stability of the high-pressure phase under UV light. The high chemical stability is a positive feature in long-term utilization of photocatalysts for different reaction such as water splitting or CO_2 conversion[5].

Computational Results

To understand the high light absorbance and high photocatalytic activity of the HPT-processed sample, three main

points were examined by DFT calculations. First, the bandgap of the columbite phase was compared with other TiO_2 polymorphs. Second, the effect of oxygen vacancies in columbite on the reduction of optical bandgap (i.e. enhanced light absorbance) was computed. Third, the surface activity of the columbite phase for water splitting was examined and compared with the activity of anatase and rutile reported in the literature.

Electronic Bandgap for Different Polymorphs

DFT is an accurate method to carry out a comparative study for the electronic structure of materials; however, DFT tends to erroneously underestimate the bandgap due to delocalized charge distribution[30–32]. To deal with this underestimation, DFT+U was used in this study for the estimation of the bandgap of columbite. The DFT+U results were first compared with the experimentally known bandgaps for anatase (3.2 eV), rutile (3.0 eV) and brookite (3.4 eV)[3,6,33,34] to determine the most reasonable U value. After the selection of the U value, the bandgap of columbite was calculated. A summary of the calculated bandgaps obtained by the variation of U values is
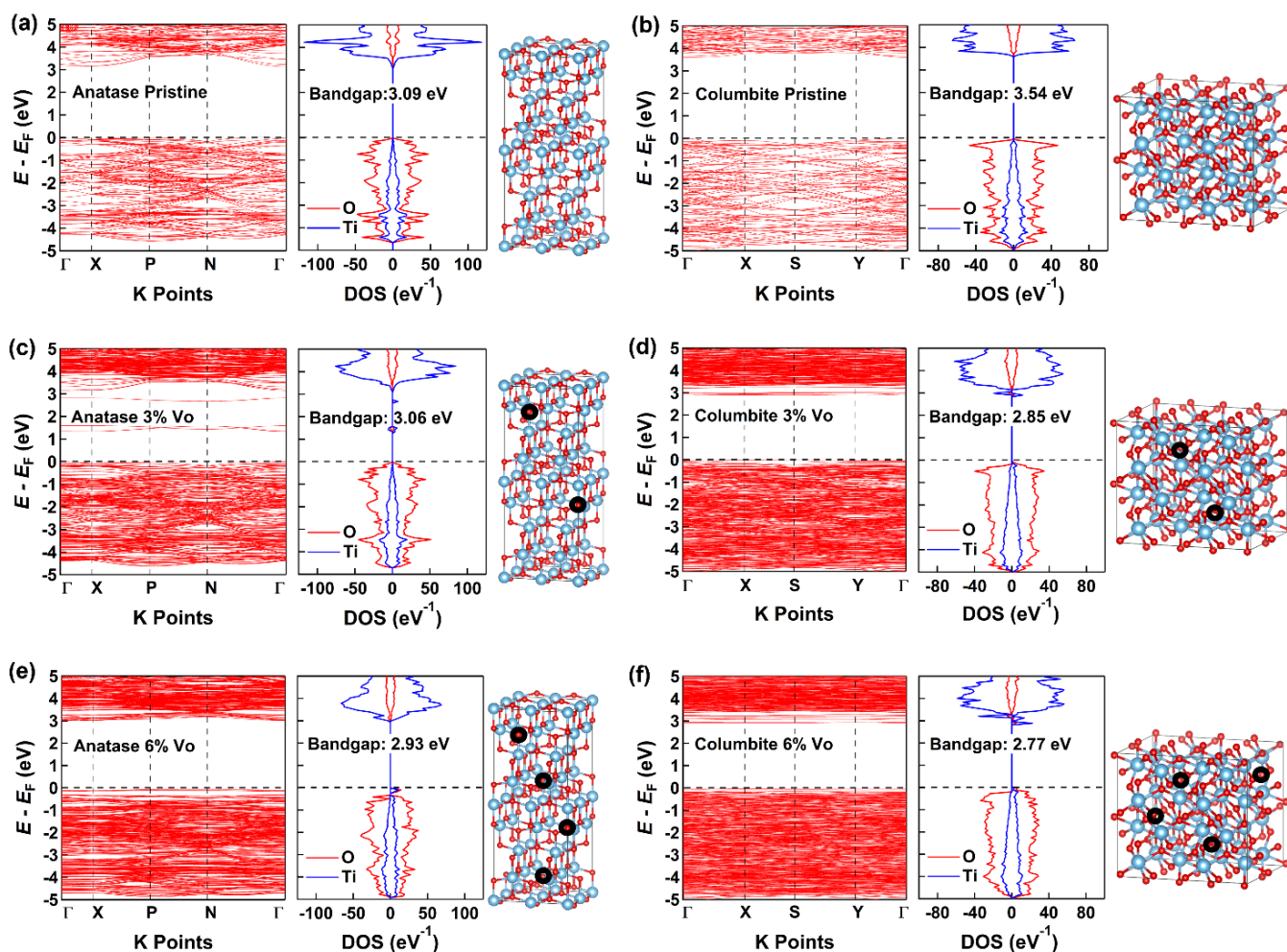
Fig. 12. Reduction of optical bandgap of columbite by oxygen vacancies. Calculated DOS and band structure and corresponding modelled supercells using U value of 8 eV for anatase with (a) 0, (c) 3 and (e) 6 at% of oxygen vacancies and for columbite with (b) 0, (d) 3, (f) 6 at% of oxygen vacancies. Dotted vertical lines represents Fermi level (E_F) and black circles in supercells show oxygen vacancy positions.

shown in Fig. 10, indicating an increase in the bandgap with increasing the U value. As a result of the comparison between the experimental bandgaps and calculated data, the U values that reach the experimental bandgap are 8 eV for anatase and brookite, and 9 eV for rutile. These U values also coincide with the reported values by other researchers for TiO_2[32,35]. Therefore, a U value of 8 eV was utilized in all calculations in this study.

Fig. 11 shows a comparison between DOS plots using a U value of 8 eV. These plots indicate three major points. (i) The valence band is mostly composed of oxygen 2p orbitals while the conduction band is composed of titanium 3d orbitals. (ii) Hybridizing orbitals can be observed near 6 eV. (iii) The bandgap of columbite by utilizing a U value of 8 eV is estimated as 3.4 eV, indicating that columbite is not a low-bandgap semiconductor and its high light absorbance and good photocatalytic activity should be influenced by other factors, as will be discussed below. Moreover, the baddeleyite phase, which was reported as a low-bandgap polymorph in an earlier theoretical study[36], appears to be a wide-bandgap semiconductor as well.

Oxygen Vacancy Effect on Electronic Structure

The experimental results showed that the HPT process produces various lattice defects in TiO_2 and defects play an important role in different reactions due to the alterations of the electronic structure of the materials. In this section, oxygen vacancies as the most effective defects in photocatalysis are studied by DFT calculations. The effect of different oxygen vacancy concentrations on the DOS and band structure in columbite is compared with anatase. For these calculations, 2 and 4 oxygen atoms were randomly removed from the structure representing 3 and 6 at% of oxygen vacancies (Vo), respectively. DOS plots are shown in Fig. 12 for (a, c, e) anatase and (b, d, f) columbite. For anatase with 3% Vo (Fig. 12(c)), two defect states are formed: (i) shallow defect states near the conduction band and (ii) deep defect states. Nonetheless, the deep defect state disappears, and shallow defect states merge with the conduction band by increasing the percentage of oxygen vacancies to 6% (Fig. 12(e)). In columbite with 3 and 6% Vo, only shallow states merged with the bottom of the conduction band

Table 1. Calculated oxygen vacancy formation energy in bulk and on surface of anatase and columbite in comparison with reported data in literature.

Vo	Phase	Position	Calculation Method	EVacancy (eV)	Ref.
12.5%	Anatase	(101)	GGA+U (3.5 eV)	4.69	[16]
25%	Anatase	(101)	GGA+U (3.5 eV)	4.88	[16]
37.5%	Anatase	(101)	GGA+U (3.5 eV)	5.04	[16]
2.08%	Anatase	(101)	GGA+U (6 eV)	5.26	[37]
4.16%	Anatase	(101)	GGA+U (6 eV)	5.14	[37]
6.25%	Anatase	(101)	GGA+U (6 eV)	5.28	[37]
8.33%	Anatase	(101)	GGA+U (6 eV)	5.06	[35]
	Anatase	Bulk	GGA+U (4.2 eV)	4.23	[39]
5.55%	Anatase	(101)	GGA+U (3 eV)	4.14	[40]
12.5%	Anatase	Bulk	HSE06	6.6	[41]
6.25%	Anatase	Bulk	HSE06	6.4	[41]
3.12%	Anatase	Bulk	HSE06	6.2	[41]
1.56%	Anatase	Bulk	HSE06	5.2	[41]
	Anatase	Bulk	HSE	4.27	[42]
	Anatase	(101)	HSE	4.37	[42]
	Anatase	(001)	HSE	4.74	[42]
	Anatase	(101)	HSE06	4.81	[43]
	Anatase	Bulk	HSE06	5.46	[43]
3%	Anatase	Bulk	GGA+U (8 eV)	5.85	This study
3%	Columbite	Bulk	GGA+U (8 eV)	3.15	This study

are observed. The shallow states merged with the conduction band are the result of Ti^{3+} formation due to extra electrons left by oxygen vacancies[5,16,37,38]. For both anatase and columbite, the optical bandgap decreases by increasing the concentration of oxygen vacancies, but the reduction is more significant for the columbite phase. The presence of oxygen vacancies and Ti^{3+} cations together with narrowing the optical bandgap have a positive effect on the photocatalytic activity of TiO_2[16,39].

To clarify the thermodynamics of the generation of oxygen vacancies in columbite, its oxygen vacancy formation energy was also calculated by utilizing Equation 1 and compared with anatase.

$$E_{\text{Vacancy}} = \frac{(E_{\text{Defect}} + n\mu_0) - E_{\text{Pristine}}}{n} \qquad (1)$$

where E_{Defect} represents the energy calculated by SCF for the structure with 3% Vo, E_{Pristine} represents the energy for the pristine structure with no defects, μ_0 is the chemical potential and n is the number of vacancies per supercell. The calculated oxygen vacancy formation energy for anatase and columbine is given in Table 1 in comparison with some reported data in the literature[16,37,39-42]. The calculated energy for anatase has good agreement with the reported data by previous researchers, while columbite has a lower oxygen vacancy formation energy than anatase. When E_{Vacancy} is less positive, the formation of vacancies is energetically more favorable, and thus, columbite should have a higher susceptibility to oxygen vacancy formation.

Surface Activity for Water splitting

The calculations for water splitting reactions were performed on the surface of (101) and (011) atomic planes of columbite. These two surfaces were selected because they were reported as the most active ones for anatase and rutile[16,17,37,44,45]. The water adsorption was performed by attaching a water molecule to a five-coordinated titanium atom and the adsorption energy ($E_{\text{Adsorption}}$) was calculated according to Equation 2.

$$E_{\text{Adsorption}} = E_{(\text{Slab}+\text{H2O})} - (E_{\text{H2O}} + E_{\text{Slab}}) \qquad (2)$$

where E_{H2O} is the energy calculated for the water molecule in vacuum, E_{Slab} is the energy of the slab, and $E_{(\text{Slab + H2O})}$ is the total energy of the system after H_2O is absorbed on the slab. For the slab (011), the adsorption energy was +10 eV which implies that the bond between the water molecule and the surface is thermodynamically unfavorable. On the other hand, the adsorption energy calculated for slab (101) was -1.67 eV, suggesting that the columbite slab (101) can absorb the water molecule on the surface. Similar calculations for anatase slab (101) led to an adsorption energy of -0.96 eV indicating that water adsorption on columbite is more energetically favorable.

Following the water adsorption calculations, reaction pathways for water splitting ($H_2O \rightarrow H+OH$) were calculated by the NEB and CiNEB methods. The NEB and CiNEB calculations for water splitting reactions on slab (011) and (101) are shown in detail in Fig. 13. In the case of (011) shown in Fig. 13(a), the energy barrier for the reaction is 0.04 eV, and the energy difference between the adsorption and dissociative states is +0.01 eV. Therefore, despite the small energy barrier, the water-splitting reaction on this atomic plane may not be energetically favorable considering the DFT calculations are conducted at absolute temperature. The energy barrier for slab (101) shown in Fig. 13(b) indicates that the water molecule can follow the proposed

reaction path. The energy barrier for the reaction is 0.013 eV and the energy difference from the first to the last step is -0.07 eV, which suggests that the reaction on the slab (101) is thermodynamically exothermic and energetically favorable.

Phonon calculations of the saddle points of the hydrogen evolution reaction on columbite atomic planes (011) and (101) of Fig. 13 are shown in Fig. 14. It is evident that saddle points for both atomic planes show imaginary phonon frequencies, indicating the dynamic instability of the saddle point[21]. These phono calculations confirms that the catalytic reaction in Fig. 13 goes through a saddle point in which an energy barrier exists between the initial (H_2O) and final (H+OH) points of reaction pathway.

The water-splitting reaction energy barriers calculated for columbite (101) confirm the high surface activity of this high-pressure phase for water splitting. Table 2 presents the values reported for energy barriers for different TiO_2 slabs of anatase and rutile[16–18,46–51] and compares them with the columbite phase. Comparatively, the energy barrier for water splitting of columbite slab (101) is smaller than those reported for the active slabs of anatase and rutile. It is concluded that the columbite phase provides high surface activity for the formation of H and OH groups which can accordingly take part in the formation of H_2 and O_2 molecules in the presence of appropriate co-catalysts.
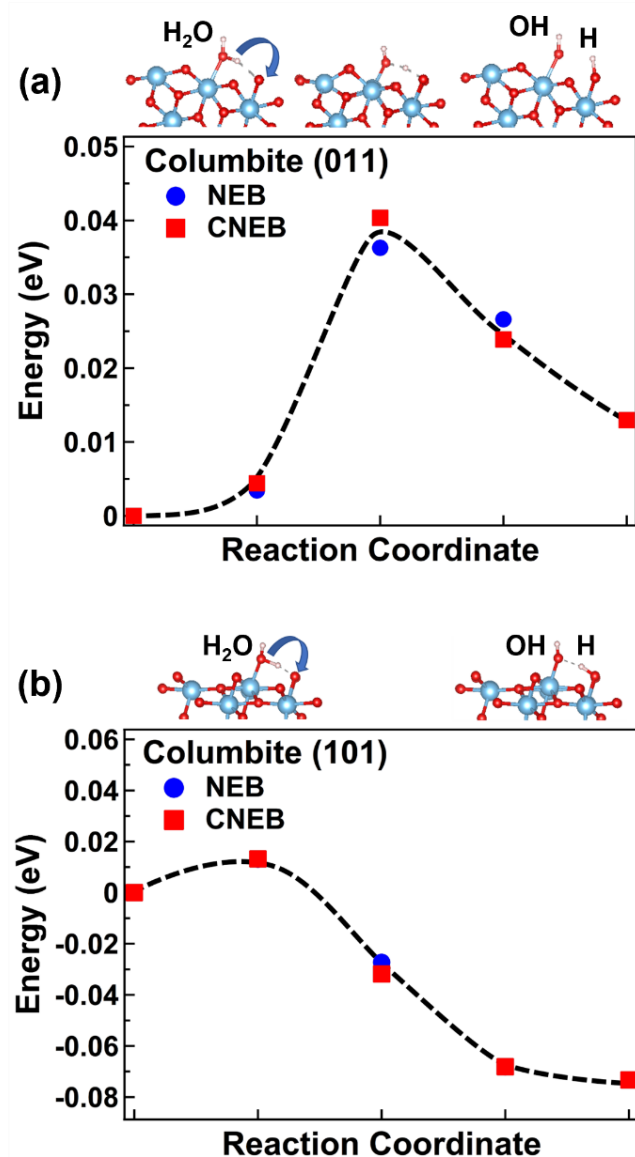
Discussion

Fig. 13. High surface activity of (101) atomic plane of columbite for water splitting reaction. Reaction pathways for water splitting on (a) (011) and (b) (101) atomic planes of columbite calculated with *U* value of 8 eV. Pathway for three main steps of water splitting ($H_2O \rightarrow H+OH$) on TiO_2 is shown on top of each plot.
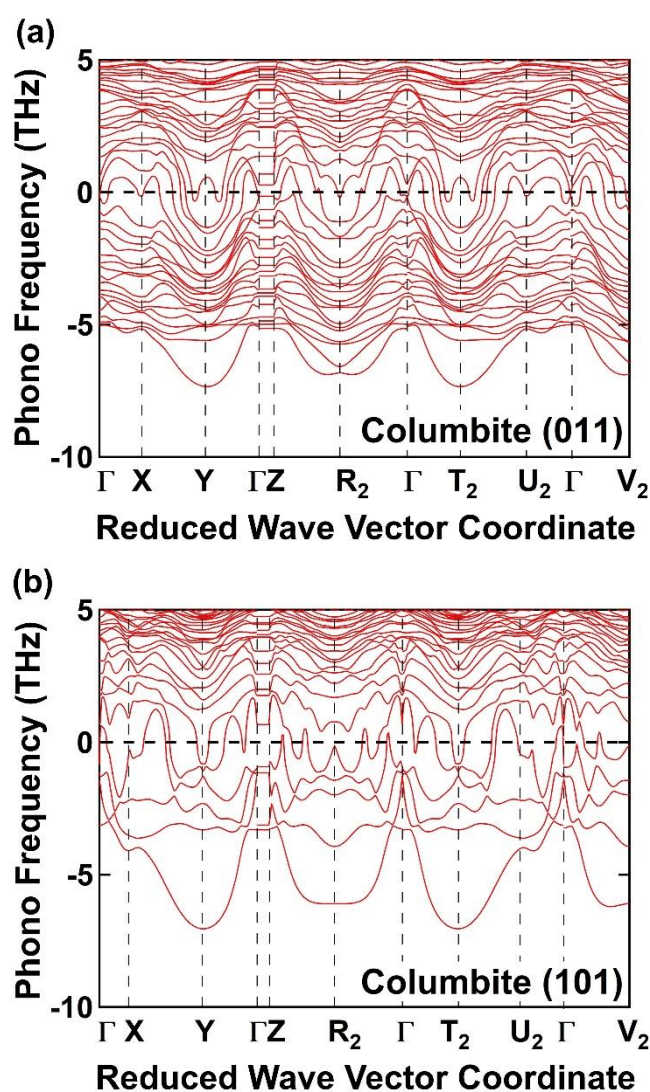

Fig. 14. Dynamic instability at saddle points of hydrogen evolution reactions of Fig. 13. Phonon dispersion curves at saddle points of water-to-hydrogen reaction over the columbite atomic planes (a) (011) and (b) (101). Imaginary modes are shown in negative values.

Table 2. Calculated energy difference and energy barrier for water splitting reaction on (101) and (011) atomic planes of columbite in comparison with reported data for TiO$_2$ anatase and rutile.

	Method	Energy Barrier (eV)	Ref.
Anatase (101)	GGA	0.02	[16]
Rutile (110)	GGA	0.16	[17]
Rutile (001)	GGA	0.109	[17]
Rutile (100)	GGA	0.225	[17]
Rutile 011	GGA	<0.1	[18]
Anatase (101)	GGA	2.67	[46]
Rutile (110)	GGA+U	0.92	[48]
Rutile (110)	GGA	0.2	[49]
Rutile (110)	GGA + U	0.12	[49]
Rutile (110)	GGA	0.28	[50]
Anatase (101)	GTH*	0.52	[51]
Anatase (001)	GTH*	0.05	[51]
Anatase (100)	GTH*	0.22	[51]
Columbite (011)	GGA	0.044	This study
Columbite (101)	GGA	0.013	This study

The experiments conducted in this study show that the high-pressure columbite phase is beneficial for the enhancement of light absorbance and the improvement of photocatalytic activity for hydrogen production from water. A large fraction of oxygen-deficient columbite (69 wt%) was stabilized by severe straining via the HPT method, which is larger than those reported in earlier studies[6,7]. Considering these experimental results three possible mechanisms were theoretically investigated: (i) the electronic bandgap of columbite, (ii) the effect of oxygen vacancies on light absorbance and bandgap, and (iii) the surface activity of columbite for water splitting reaction.

Based on the findings of the bandgap calculations using different U values, it was possible to determine that the columbite does not have a lower bandgap than other TiO$_2$ polymorphs. These calculations, which were in good agreement with the reported calculations for anatase and rutile[16,36,41,46], do not support an earlier DFT study that suggested high-pressure TiO$_2$ phases as a low-bandgap semiconductor[34]. Therefore, examination of the first mechanism confirms that enhanced light absorbance and good photocatalytic activity of HPT-processed TiO$_2$ cannot be attributed to a decrease in the electronic bandgap. Oxygen vacancies, especially on the surface are considered highly reactive sites which can enhance photon absorption, photogenerated electron-hole separation, chemical adsorption, reactant molecule activation and ionic conductivity[7,16,38–40,46,47,51]. The effect of oxygen vacancies in anatase and rutile was extensively studied earlier[16,37–43,47,53,54], however, few studies were conducted to clarify the effect of oxygen vacancies on the high-pressure columbite phase. The theoretical calculations in this study confirm that oxygen vacancies in both anatase and columbite can narrow the optical bandgap by merging the defect states with the conduction band. However, a higher bandgap narrowing by oxygen vacancies occurs in columbite which has a higher atomic density per volume unit. These computational results (Fig. 12) reasonably justify the experimental results for higher light absorbance and lower optical bandgap of HPT-processed TiO$_2$ (Fig. 6). It is concluded that a combination of high-pressure phase and oxygen vacancy generation is essential to achieve good light absorbance in TiO$_2$. Based on the oxygen vacancy formation energy summarized in Table 2, vacancy formation in columbite is

energetically more favorable compared to the anatase phase[16-18,46-51], and this can be beneficial to develop oxygen-deficient columbite for water splitting.

In addition to light absorbance, surface chemical absorbance and chemical activity are other key factors to improve photocatalytic activity. The computations show that water absorbance to the (101) surface of columbite is energetically favorable. Moreover, the (101) surface of columbite shows a lower energy barrier for water splitting compared to the active surfaces of anatase and rutile, as summarized in Table 1[16–18,46–51]. Taken together, a combination of high light absorbance and chemical absorbance and surface activity is responsible for the high activity of oxygen-deficient columbite. Although oxygen vacancies in bulk may act as recombination centers of charge carriers[6,7,48,55], the presence of surface oxygen vacancies, multiple phases and formation of heterojunctions after HPT processing is expected to contribute to diminishing the recombination of charge carriers[25,26]. Among these features oxygen vacancy engineering was employed more widely in developing various active photocatalysts[56,57]. Lower electron-hole recombination after HPT processing, which is expected from the low intensity of PL spectra in Fig. 7 and high photocurrent intensity in an earlier work[7], can also contribute to the high photocatalytic activity. Despite the high potential of the oxygen-deficient columbite phase for photocatalytic hydrogen production, its synthesis method needs to be improved in the future to produce a large quantity of the catalyst with a large surface area. Moreover, other strategies used to generate active sites and enhance the photocatalytic activity of different TiO$_2$ polymorphs (e.g. adding dopants, making porosity, generating facets, etc.)[58–60] can be employed in the future to further improve the photocatalytic activity of columbite.

Conclusions

A combination of quantum mechanical calculations and experiments was used to understand the high photocatalytic activity of the oxygen-deficient high-pressure columbite phase. The main conclusions can be summarized as follows.

(1) The results of bandgap calculations for different TiO$_2$ polymorphs indicate that columbite is not a low-bandgap catalyst.

(2) Calculations suggest that columbite has a lower vacancy formation energy, and oxygen vacancies can decrease its optical bandgap more significantly compared to anatase, a fact that was experimentally confirmed by light absorbance and optical bandgap measurements.

(3) The (101) surface of columbite demonstrates a high tendency for the water molecule absorbance and a low activation energy for water splitting to H and OH, a fact that was experimentally confirmed by photocatalytic hydrogen production.

Conflicts of interest

There are no conflicts to declare.

Acknowledgements

References

1   A. Kudo and Y. Miseki, *Chem. Soc. Rev.*, 2009, **38**, 253–278.
2   K. Sasaki, H.-W. Li, A. Hayashi, J. Yamabe, T. Ogura, Hai-Wen Li, Akari Hayashi, Junichiro Yamabe, Teppei Ogura and Stephen M. Lyth, *Hydrogen Energy Engineering: A Japanese Perspective*, Springer Japan, Fukuoka, Japan, 2016.
3   A. Fujishima, R. Tata N. and D. A. Tryk, *J. Photochem. Photobiol. C Photochem. Rev.*, 2000, **1**, 1–21.
4   D. A. H. Hanaor and C. C. Sorrell, *J. Mater. Sci.*, 2011, **46**, 855–874.
5   S. K. Cushing, F. Meng, J. Zhang, B. Ding, C. K. Chen, C. J. Chen, R. S. Liu, A. D. Bristow, J. Bright, P. Zheng and N. Wu, *ACS Catal.*, 2017, **7**, 1742–1748.
6   H. Razavi-Khosroshahi, K. Edalati, M. Hirayama, H. Emami, M. Arita, M. Yamauchi, H. Hagiwara, S. Ida, T. Ishihara, E. Akiba, Z. Horita and M. Fuji, *ACS Catal.*, 2016, **6**, 5103–5107.
7   S. Akrami, M. Watanabe, T. H. Ling, T. Ishihara, M. Arita, M. Fuji and K. Edalati, *Appl. Catal. B Environ.*, 2021, **298**, 120566.
8   K. Edalati, Z. Horita, *Mater. Sci. Eng. A*, 2016, 652, 325–352.
9   Q. Wang, K. Edalati, Y. Koganemaru, S. Nakamura, M. Watanabe, T. Ishihara, Z. Horita, *J. Mater. Chem. A*, 2020, 8, 3643–3650.
10 P. Kubelka and F. Munk, *Zeitschrift für Tech. Phys.*, 1931, **12**, 593–601.
11 G. Kresse and J. Furthmüller, *Phys. Rev. B - Condens. Matter Mater. Phys.*, 1996, **54**, 11169–11186.
12 G. Kresse and J. Hafner, *Phys. Rev. B*, 1993, **47**, 558–561.
13 P. E. Blöchl, *Phys. Rev. B*, 1994, **50**, 17953–17979.
14 K. Momma and F. Izumi, *J. Appl. Crystallogr.*, 2011, **44**, 1272–1276.
15 K. Brlec, D. Davies and D. Scanlon, *J. Open Source Softw.*, 2021, **6**, 3171.
16 S. Jia, J. Gao, Q. Shen, J. Xue, Z. Zhang, X. Liu and H. Jia, *J. Mater. Sci. Mater. Electron.*, 2021, **32**, 13369–13381.
17 Z. Y. Zhao, *J. Phys. Chem. C*, 2014, **118**, 4287–4295.
18 U. Aschauer and A. Selloni, *Phys. Rev. Lett.*, 2011, **106**, 1–4.
19 J. Balajka, U. Aschauer, S. F. L. Mertens, A. Selloni, M. Schmid and U. Diebold, *J. Phys. Chem. C*, 2017, **121**, 26424–26431.
20 G. Henkelman, B. P. Uberuaga and H. Jónsson, *J. Chem. Phys.*, 2000, **113**, 9901–9904.
21 A. Togo, I. Tanaka, *Scr. Mater.*, 2015, **108**, 1–5.
22 K. Edalati, A. Bachmaier, V. A. Beloshenko, Y. Beygelzimer, V. D. Blank, W. J. Botta, K. Bryła, J. Čížek, S. Divinski, N. A. Enikeev, Y. Estrin, G. Faraji, R. B. Figueiredo, M. Fuji, T. Furuta, T. Grosdidier, J. Gubicza, A. Hohenwarter, Z. Horita, J. Huot, Y. Ikoma, M. Janeček, M. Kawasaki, P. Král, S. Kuramoto, T. G. Langdon, D. R. Leiva, V. I. Levitas, A. Mazilkin, M. Mito, H. Miyamoto, T. Nishizaki, R. Pippan, V. V. Popov, E. N. Popova, G. Purcek, O. Renk, Á. Révész, X. Sauvage, V. Sklenicka, W. Skrotzki, B. B.

23 Straumal, S. Suwas, L. S. Toth, N. Tsuji, R. Z. Valiev, G. Wilde, M. J. Zehetbauer and X. Zhu, *Mater. Res. Lett.*, 2022, **10**, 163–256.
23 K. Edalati, *Adv. Eng. Mater.*, 2019, **21**, 1800272
24 G. E. Dieter, *Mech. Metall.*, 1961.
25 K. Afroz, M. Moniruddin, N. Bakranov, S. Kudaibergenov, N. Nuraje, *J. Mater. Chem. A*, 2018, **6**, 21696–21718.
26 P. Edalati, Y. Itagoe, H. Ishihara, T. Ishihara, H. Emami, M. Arita, M. Fuji, K. Edalati. *J. Photochem. Photobiolo. A.* 2022, **433**, 114167.
27 S. Akrami, Y. Murakami, M. Watanabe, T. Ishihara, M. Arita, Q. Guo, M. Fuji, K. Edalati, *J. Chem. Eng.*, 2022, **442**, 136209.
28 I. Fujita, P. Edalati, Q. Wang, M. Watanabe, M. Arita, S. Munetoh, T. Ishihara, K. Edalati, *Scr. Mater.*, 2020, **187**, 366–370.
29 D. K. Pallotti, L. Passoni, P. Maddalena, F. Di Fonzo and S. Lettieri, *J. Phys. Chem. C*, 2017, **121**, 9011–9021.
30 M. Shishkin and H. Sato, *J. Chem. Phys.*, 2019, **151**, 024102.
31 V. I. Anisimov, F. Aryasetiawan and A. I. Lichtenstein, *J. Phys. Condens. Matter*, 1997, **9**, 767–808.
32 M. E. Arroyo-De Dompablo, A. Morales-Garca and M. Taravillo, *J. Chem. Phys.*, 2011, **135**, 054503.
33 J. Zhang, P. Zhou, J. Liu and J. Yu, *Phys. Chem. Chem. Phys.*, 2014, **16**, 20382–20386.
34 W. Hu, L. Li, G. Li, C. Tang and L. Sun, *Cryst. Growth Des.*, 2009, **9**, 3676–3682.
35 M. T. Curnan and J. R. Kitchin, *J. Phys. Chem. C*, 2015, **119**, 21060–21071.
36 T. Zhu and S. P. Gao, *J. Phys. Chem. C*, 2014, **118**, 11385–11396.
37 N. S. Portillo-Vélez, O. Olvera-Neria, I. Hernández-Pérez and A. Rubio-Ponce, *Surf. Sci.*, 2013, **616**, 115–119.
38 N. Hamamoto, T. Tatsumi, M. Takao, T. Toyao, Y. Hinuma, K. I. Shimizu and T. Kamachi, *J. Phys. Chem. C*, 2021, **125**, 3827–3844.
39 B. J. Morgan and G. W. Watson, *J. Phys. Chem. C*, 2009, **113**, 7322–7328.
40 Y. Hinuma, T. Toyao, T. Kamachi, Z. Maeno, S. Takakusagi, S. Furukawa, I. Takigawa and K. I. Shimizu, *J. Phys. Chem. C*, 2018, **122**, 29435–29444.
41 M. Elahifard, M. R. Sadrian, A. Mirzanejad, R. Behjatmanesh-Ardakani and S. Ahmadvand, *Catalysts*, 2020, **10**, 397.
42 H. Li, Y. Guo and J. Robertson, *J. Phys. Chem. C*, 2015, **119**, 18160–18166.
43 P. Deák, J. Kullgren and T. Frauenheim, *Phys. Status Solidi - Rapid Res. Lett.*, 2014, **8**, 583–586.
44 Z. Futera, N.J. English, *J. Phys. Chem. C,* 2017, **121**, 6701–6711.
45 T. Luttrell, S. Halpegamage, J.Tao, A. Kramer, E. Sutter, M. Batzill, *Sci. Rep.,* 2014, **4**, 4043.
46 Z. Li, X. Zhang, L. Zhang, C. Xu and Y. Zhang, *J. Phys. Chem. C*, 2020, **124**, 26214–26221.
47 S. Wendt, R. Schaub, J. Matthiesen, E. K. Vestergaard, E. Wahlström, M. D. Rasmussen, P. Thostrup, L. M. Molina, E. Lægsgaard, I. Stensgaard, B. Hammer and F. Besenbacher, *Surf. Sci.*, 2005, **598**, 226–245.
48 K. K. Ghuman, *Sci. Technol. Adv. Mater.*, 2018, **19**, 44–52.
49 Y. Ji, B. Wang and Y. Luo, *J. Phys. Chem. C*, 2014, **118**, 1027–1034.
50 Q. Guo, C. Xu, Z. Ren, W. Yang, Z. Ma, D. Dai, H. Fan, T. K. Minton and X. Yang, *J. Am. Chem. Soc.*, 2012, **134**, 13366–13373.
51 J. Q. Li, Y. Sun and J. Cheng, *J. Mater. Chem. A*, 2023, 943–952.
52 H. E. Wang, K. Yin, N. Qin, X. Zhao, F. J. Xia, Z. Y. Hu, G. Guo, G. Cao and W. Zhang, *J. Mater. Chem. A*, 2019, **7**, 10346–10353.
53 L. Mino, G. Spoto and A. M. Ferrari, *J. Phys. Chem. C*, 2014, **118**, 25016–25026.
54 H. Heydari, M. R. Elahifard and R. Behjatmanesh-Ardakani, *Surf. Sci.*, 2019, **679**, 218–224.

55 J. Yan, G. Wu, N. Guan, L. Li, Z. Li and X. Cao, *Phys. Chem. Chem. Phys.*, 2013, **15**, 10978–10988.

56 Z. Sun, T. Liu, Q-. Shen, H. Li, X. Liu, H. Jia, J. Xue, *Appl. Surf. Sci*, 2023, **616**, 156530.

57 J. Gao, J. Xue, Q. Shen, T. Liu, X. Zhang, X. Liu, Q. Li, Y. Wu, *Chem. Eng.*, 2022, **431**, 133281.

58 M. Liu, L. Piao, L. Zhao, S. Ju, Z. Yan, T. He, C. Zhou, W. Wang, *Chem. Commun.,* 2010, **46,** 1664–1666.

59 M. Liu, X. Qiu, M. Miyauchi, K. Hashimoto, *J. Am. Chem. Soc.*, 2013, **135**, 10064–10072.

60 S. Cao, T. S. Chan, Y. R. Lu, X. Shi, B. Fu, Z. Wu, H. Li, K. Liu, S. Alzuabi, P. Cheng, M. Liu, T. Li, X. Chen, L. Piao, *Nano Energy,* 2020, **67**, 104287.
.